ECS Transactions, 33 (16) 227-243 (2011)
10.1149/1.3553173 ©The Electrochemical Society

Corrosion Inhibition of 304 Stainless Steel, Copper and Nickel Metals Using Mesoporous Silicate (MCM- 41) and 2, 5- Distyrylpyrazine Photopolymer

M. B. Zakaria [a], M. A. Elmorsi [a], and E. M. Ebeid [a, b]

[a] Department of Chemistry, Faculty of Science, Tanta University, Tanta, Egypt
[b] Misr University for Science and Technology (MUST), 6th of October City, Egypt

Mesoporous silicate (MCM-41) and 2, 5-distyrylpyrazine photo-polymer (poly-DSP) were used as corrosion protective coatings for 304 stainless steel, copper and nickel metals. Films on metal surfaces were prepared by dip-coating and vapor deposition (CVD, PVD) methods. Poly-DSP thin films formed by vapor deposition are expected to be incorporated through pores and micro-cracks of SiO_2 thin film resulting in extra corrosion protection upon photo polymerization. MCM-41 thin films were characterized by x-ray diffraction (XRD), infrared (IR), BET and electron microscopy (SEM, TEM) techniques. Corrosion protection was studied in 2M HCl aqueous solutions using weight loss and potentiodynamic polarization techniques. The temperature effect on corrosion rates was also studied and the thermodynamic activation parameters of the corrosion reaction were determined. Different corrosion parameters were evaluated including, corrosion current density, corrosion potential, corrosion rate and Tafel constants. The calculated percentage of inhibition efficiencies of the coated electrodes reaches ca 93% in some cases.

Introduction

A general method to enhance corrosion resistance is to apply protective coatings. The modification of the chemical composition of the coatings can also permit the introduction of other desired chemical and physical properties, such as mechanical strength and hydrophobicity. Various organic coatings have been studied for corrosion protection (1-3). Various oxide coatings obtained by sol-gel processing have been studied extensively for corrosion protection of stainless steel (4-8). In spite of all advantages of sol-gel processing, sol-gel coatings suffer from several drawbacks. Specifically, the high annealing or sintering temperatures (>800 ^{0}C) required to achieve a dense microstructure could possibly introduce cracks and/or delamination within the sol-gel coatings (9-12). One viable approach to dense sol-gel derived coatings without post- deposition annealing at elevated temperature is to synthesize organic-inorganic hybrid coatings. Relatively dense hybrid coatings have been developed for applications, including wear resistance (13, 14) and corrosion protection (15-17). Two common methods for preparing coatings on metal surfaces are gaseous, including physical vapor deposition (PVD) and chemical vapor deposition (CVD) methods (18, 19), and liquid phase (20, 21) methods. Most of the ceramic coatings are formed by sol-gel method which requires considerably less equipment and can be amenable to any accessories in a large and complex shape, and is applicable to substrates that cannot withstand high temperatures (22). However, the coatings fabricated by sol-gel process encounter problems of existing pores and cracks

which may become a detrimental factor to cause delamination and corrosion at the interface of coating and substrates (23). The interest in the sol-gel method for preparation of protective coatings of metallic substrates has nonetheless increased in the last ten years. SiO_2 coatings made from tetraethoxysilane (TEOS) have been proposed as oxidation protection of metals since it is one of the best barriers against oxygen diffusion. Although the electrochemical response of these coating is poor due to the presence of residual porosity or micro-cracks that enable the access of the electrolyte to the substrate, the use of alkylalcoxides as precursors effectively improved the performance of these coatings (24). Polymer coatings such as polypyrrole, polyaniline, polyvinyl alcohol, polyethylene glycol, poly(methylmethacrylate) .. etc. have been shown to offer corrosion protection of ferrous and non-ferrous metals (25). Kinlen et al. (26, 27) have shown that polyaniline (PANI) containing organic coating on steel is able to passivate the pinholes and defects in the coating and causes passivation of metal surface through anodization of metal by PANI and formation of an insoluble iron-dopant salt at the metal surface. The inhibition efficiencies of other polymers like polyvinyl alcohol (PVA) and polyethylene glycol (PEG) were evaluated using the weight loss and hydrogen evolution techniques at 30-60°C (28). 2, 5- distyrylpyrazine monomer (DSP) is known to undergo four - center type photopolymerization giving highly crystalline 2, 5- distyrylpyrazine photopolymer (poly-DSP) (29). In this article, 2, 5- distyrylpyrazine monomer was incorporated by physical vapor deposition (PVD) in pores and micro-cracks of SiO_2 thin films followed by its photo polymerization. This offered extra corrosion protection of stainless steel, copper and nickel metals.

Experimental

Preparation of mesoporous silicate (MCM 41)

Chemicals. Tetraethyloxysilane (TEOS) (99%) was purchased from Merck. Cetyltrimethyl ammonium bromide (CTAB) (99%) and sodium hydroxide (NaOH) (98%) were purchased from Fluka.

Procedures. 0.46 g NaOH was dissolved into 120 ml H_2O with stirring. After the solution becomes clear, 1.4 g CTAB was dissolved completely, and 5.6 ml TEOS was poured into the above solution under vigorous stirring. Stirring was continued for 24 h, and then the mixture was heated at 80 ºC for 48 h. The mixture was filtered to obtain the silicate solid particles, dried at 100 ºC for 6 h and the surfactant was removed by calcination at 550 ºC for 5 h (30).

Fabrication of mesoporous silicate (MCM-41) thin films

In the preparation of a uniform nano coating, the pretreatment of the substrate surfaces is important. The metal sheet (2 cm×1 cm) was gradually ground using No. 320-1500 emery papers , polished with Al_2O_3 powder, and then ultrasonically cleaned in acetone , ethanol , and distilled water for 10 min, respectively. After hot air drying, it was coated with nanoparticles. Metal sheets were coated with mesoporous silicate coatings by dip-coating method. In this procedure, the substrate was immersed in the sol solution for 5 minutes then withdrawn at a speed of 0.5-1 mm/s. After drying naturally in the ambience, the specimens were heated in an oven at 150 °C for 30 min. Such operation was repeated for four times to increase the coating thickness. Then, the samples were

heat-treated at 450 °C for 30 min to enable the oxide conversion and removal of solvent and residual organics in the coating. However, during the procedure of densification, crystallization of SiO_2 and removal of residual hydroxyl and organic groups, the nano coatings were usually prone to cracking. In order to eliminate the creak defects in the coating and to optimize the coating structure and properties, the nano-SiO_2 coated samples were immersed in a boiling water for 10-50 min, and then thermally-treated in the muffle oven again at 450 °C for 10 min.

Preparation of 2, 5- distyryl pyrazine (DSP) monomer and poly- DSP thin films

2, 5- distyrylpyrazine (DSP) monomer was synthesized according to Probst et.al. (31) using 2, 5- bis (bromomethyl) pyrazine as a starting material. The phosphonium salt reacts with benzaldehyde to furnish the desired compound. Photopolymerization of DSP was reported by Masaki Hasegawa et al. in 1967 (32). Since then, a large number of new polymer crystals have been prepared from conjugated diolefinic crystals. All the polymers studied so far, are highly crystalline and three dimensionally oriented with the 1, 3- trans cyclobutane and 1, 4- phenylene groups alternating in the main chain (32). DSP thin films are formed through vapor deposition methods because DSP sublimes at ca. 100 ºC and is incorporated through pores and micro-cracks of SiO_2 thin films. Upon exposure to UV-light (λ=365 nm), poly-DSP thin films are formed causing extra corrosion protection.

Characterization of mesoporosus silicate (MCM-41)

The XRD experiments were performed by using PW 1729 X-ray generator. The XRD patterns were collected using Cu $K\alpha_1$ radiation (1.5405 A°) at a voltage of 40 kV and current of 30 mA.

The IR measurements were performed by using PERKIN-ELMER 1430 ratio recording infrared spectrophotometer over wave number range from (400 - 4000 cm^{-1}).

N_2 adsorption and desorption isotherms were measured at -197 °C using a Micromeritics ASAP 2010 apparatus. Prior to experiments, the samples were dehydrated at 350 °C until the vacuum pressure was below 5 μmHg. The measurement of the surface areas of the samples was achieved by Brunauer-Emmett-Teller (BET) method for relative pressures in the range P/P° = 0.0-1.0, and the pore size distributions were determined by Barrett-Joyner-Halenda (BJH) method. The BET method was used for the calculation of surface areas of mesoporous silicate surface by physical adsorption of N_2 gas molecules. The Barrett-Joyner-Halenda (BJH) method was used for calculating pore size distributions (33). The method is based on a model of the adsorbent as a collection of cylindrical pores. The theory accounts for capillary condensation in the pores using the classical Kelvin equation, which in turn assumes a hemispherical liquid-vapor meniscus and a well-defined surface tension. The BJH theory also incorporates thinning of the adsorbed layer through the use of a reference isotherm; the Kelvin equation is only applied to the “core” fluid.

TEM images were obtained on JEOL JEM-100SX Electron Microscope with field gun, and an accelerating voltage of 80 kV.

SEM images were obtained on JEOL-JSM-5200LV scanning microscope with field gun, and an accelerating voltage of 20 kV.

Corrosion measurements

Working electrodes and electrochemical cell. The working electrodes were in the form of sheets of surface area $2cm^2$ and chemical composition as shown in Tables (I - III). The electrodes preparation was described elsewhere (34). The aggressive corrosion medium was an aerated aqueous solution of 2 M HCl. The electrochemical cell assembly consists of a 250 ml multi-necked flask with ground glass joints to introduce a thermometer, gas inlet and outlet tubes, a saturated calomel electrode (SCE), a counter-electrode (CE) and a working electrode (WE) (34). The counter-electrode (CE) is a metal piece nobler than the sample (Pt wire) and the working electrode (WE) is the material to be analyzed (304 stainless steel, copper and nickel metals).

TABLE I. The chemical composition of 304 stainless steel sheets.

Element	C	Si	Mn	Cr	Ni	S	P	Fe
Weight %	0.05	0.5	1.4	18.4	9.50	0.03	0.045	70.075

TABLE II. The chemical composition of nickel sheets (BDH grade).

Element	Al	Co	Cu	Fe	Mn	Mg	Ti	Ni
Weight %	0.05	0.005	0.005	0.05	0.005	0.005	0.005	99.875

TABLE III. The chemical composition of copper sheets.

Element	As	Bi	Ca	Fe	Pb	Mn	Ni	K	Na	Sn	Cu
Weight%	0.001	0.0015	0.002	0.005	0.0015	0.002	0.01	0.005	0.005	0.01	99.9

Weight loss method measurements. Weight loss methods are comprehensive corrosion tests for laboratory and field. They are useful for metals and alloys which are not subjected to special types of attack and from which the products of corrosion are easily removed. Although the measurements help us to make quantitative estimate of amount of corrosion, they have many defects e.g. the error due to incomplete removal of corrosion products, loss of un-corroded metal, and the need of large number of specimens to determine a time corrosion curve properly.

To determine the percentage of inhibition efficiency of certain inhibitor using this method, the metal samples (20x10x3mm) were polished, degreased, weighed and immersed in the corrosive solution (100 ml 2M HCl) for certain time intervals at fixed temperatures. The weight loss was determined after removing the corrosion products, thoroughly washing the specimen with distilled water and drying.

The percentage of inhibition efficiency was calculated from the weight loss values using the following equation (1).

$$\% \text{ inhibition efficiency} = [(w_1-w)/w_1] \times 100 \qquad [1]$$

where w_1 and w are the weights loss of uncoated and coated samples, respectively.

Potentiodynamic polarization measurements. The Potentiodynamic polarization measurements were performed in the potential range from -2000 mV to 2000 mV vs. SCE (cover all potential range of samples under investigation), at a scan rate of 10.0 mVs^{-1} in 2 M HCl solution. The polarization curves were determined using Meinsberger Potentiostat Galvanostat PS6 with software of Potentiostat/Galvanostat PS6 with controlling software PS remote. The resulting current density is plotted on logarithmic

scale against potential. The percentage of inhibition efficiency can be obtained from the following equation (2).

$$\% \text{ inhibition efficiency} = [(I_1\text{-}I)/I_1] \times 100 \quad [2]$$

where I_1 and I are the corrosion currents of uncoated and coated samples respectively.

Results and discussion

Characterization of mesoporous silicate (MCM41)

Figure 1(a, b) shows XRD patterns for the mesoporous silicate (MCM-41) showing an amorphous material in the 2θ region between 10.0° and 35.0° (Fig. 1-a). The small angle XRD analysis of MCM-41 showed a diffraction peak at lower 2θ angles between 2.0^0 and 3.0^0 due to its hexagonal structure following calcination (Fig. 1-b).

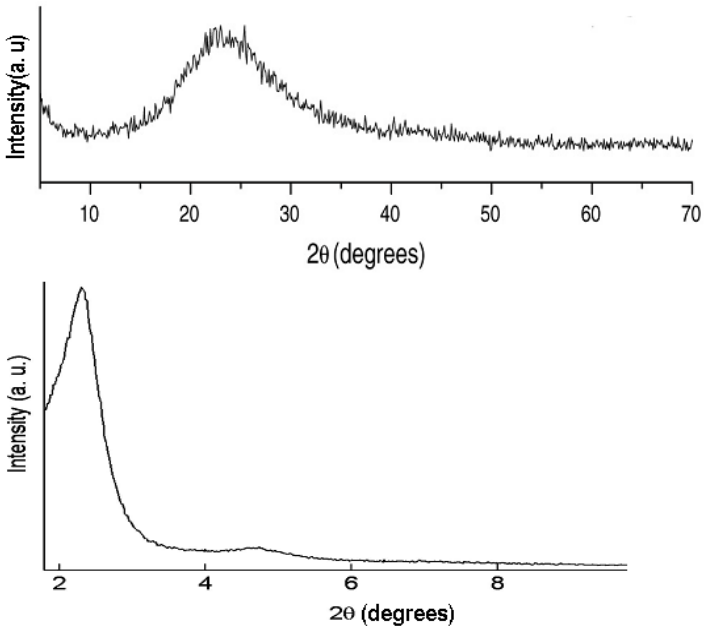

Figure 1. Large and small angle-XRD patterns for mesoporous silicate (MCM-41).

The reflections are due to the ordered hexagonal array of parallel silicate tubes and can be indexed assuming a hexagonal unit cell as (100), (110) and (200). Since the MCM-41 material is not crystalline at the atomic level, no reflections at higher angles are observed.

Figure 2 presents the IR spectra of as-synthesized and calcined MCM-41 samples. Bands at 1090 and 795 cm^{-1} belonging to the asymmetric and symmetric stretching vibrations, respectively, corresponding to the Si–O–Si framework and can be observed from the IR spectrum of the as-synthesized samples. The intense band at 3466 cm^{-1} as well as the weak band at 968 cm^{-1} represent Si–OH stretching and bending vibrations, respectively. Since the sample we prepared has been synthesized through synergistic self assembly between surfactant (CTAB) and silicate resource (TEOS) to form mesoporous ordered composites, it was formed via a condensation of silanols along the micellar surface of the surfactant .

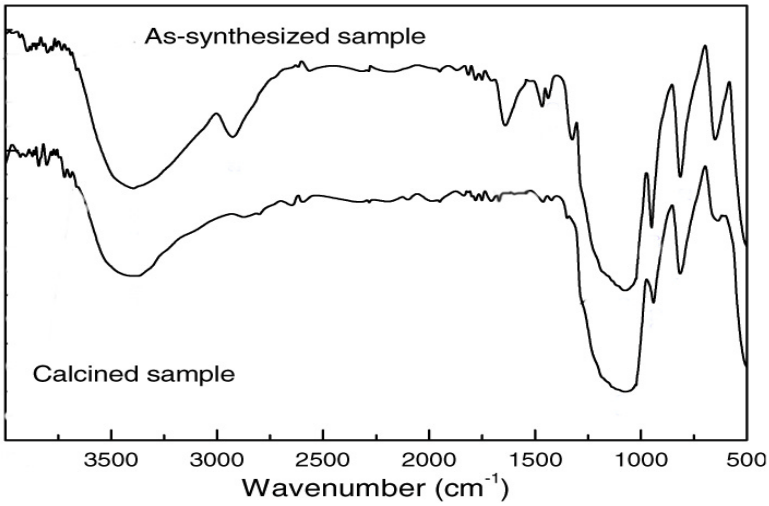

Figure 2. IR spectra of the as-synthesized and calcined MCM-41samples.

It is expected that a large quantity of silanol groups should be detected on the inorganic walls of MCM-41. It is evident that the IR spectrum of the as-synthesized samples confirms these silanol groups (Si–OH). For the calcined sample, the band at 1090 cm^{-1} becomes broad, but its position remains unchanged, and the band at 795 cm^{-1} shifts to a higher wavenumber (807 cm^{-1}) because of structural contraction, which has been confirmed by the XRD patterns of the samples as discussed in the above section. It is deduced that the condensation between the silanol groups proceeds further during the calcination process. This reduces the concentration of silanols and consequently results in a shift of the band at 795 cm^{-1} to a higher wavenumbers. Furthermore, the intensity of the absorption peak of silanol groups at 3466 cm^{-1} weakens in comparison with that of the as-synthesized sample, which is attributed to further condensation of silanols during calcination. It is also observed that absorbance peaks corresponding to C–H stretching (2850-3000 cm^{-1}) and bending (1375 and 1290 cm^{-1}) vibrations of the surfactant within the pores of the prepared mesoporous silicate have disappeared after calcination, which implies the complete removal of the surfactant.

Nitrogen adsorption-desorption probes the textural properties of materials, i.e. surface area, pore volume, pore size (distribution) and pore geometry. Moreover, the technique also discloses to what extent the measured surface area is associated with micro-, meso- and / or macropores. Figure 3 shows the nitrogen adsorption-desorption isotherms of MCM-41. The nitrogen adsorption-desorption isotherms of MCM-41 material exhibit a reversible type IV in the IUPAC classification of mesoporous materials (35).

The leap in the curve can be due to the capillary condensation of nitrogen in the channels of the mesoporous material (36). The data calculated from the curves indicate that the MCM-41 possess a narrow pore size distribution with an average pore size of about 3.38 nm which is characteristic of mesoporous materials with well ordered structure. However, the nanosilicate presents a broader pore size distribution. Table (IV) summarizes these results, and shows the different pore diameters (D_P), specific surface areas (S_{BET}), and pore volumes (V_P) for the sample. Surface areas of ca 1011.3 m^2/g were measured for pure MCM-41. Therefore, the data collected in this part of the isotherm are used for the calculation of the surface area of the material with the method developed by Brunauer, Emmett and Teller (BET-method). From the adsorption and desorption curves

pore size distributions were calculated according to the method of Barrett, Joyner and Halenda (BJH-method) which is appropriate to study changes of pore diameters.

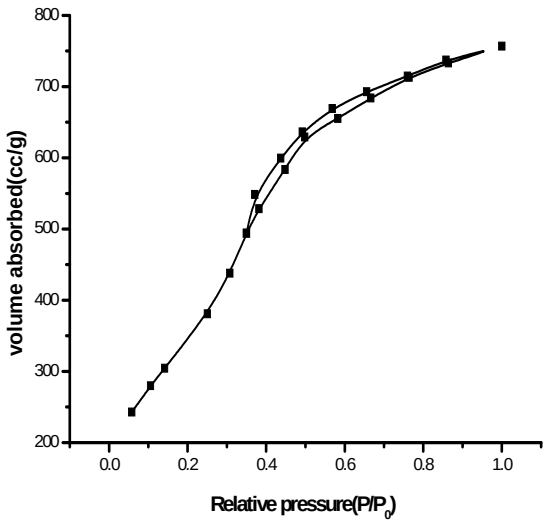

Figure 3. Nitrogen adsorption and desorption isotherms of MCM-41.

TABLE IV. Nitrogen adsorption-desorption isotherm data of MCM-41.

Sample	V_p (cm^3/g)	D_p (nm)	S_{BET} (m^2/g)
MCM-41	1.177	3.38	1011.3

Figure 4 shows the TEM images of MCM-41, allowing the viewer to look directly inside the mesopores. The mesopores are arranged in a honeycomb-like structure (Figure 4-a), separated by thin amorphous silicate pore walls (black), approximately 1-1.5 nm thick. The pore size of this MCM-41 material is approximately 3 nm in diameter. The mesopores are not necessarily running in a straight way through the silicate matrix, but they can be slightly curved, thereby retaining the hexagonal ordering, as can be seen in Figure (4-b). This increases its ability to be adsorbed and deposited into the metal surfaces forming a thin film causing corrosion inhibition. The presence of pores, cracks and channels play a role in adhering other materials like poly-DSP forming a double layer with subsequent increase of corrosion protection.

Figure 5 shows SEM images of stainless steel, copper and nickel metal surfaces coated by mesoporous silicate (MCM-41) prepared by dipping method, where MCM-41 takes spherical shape of particle size 100 nm on the surface of metals.

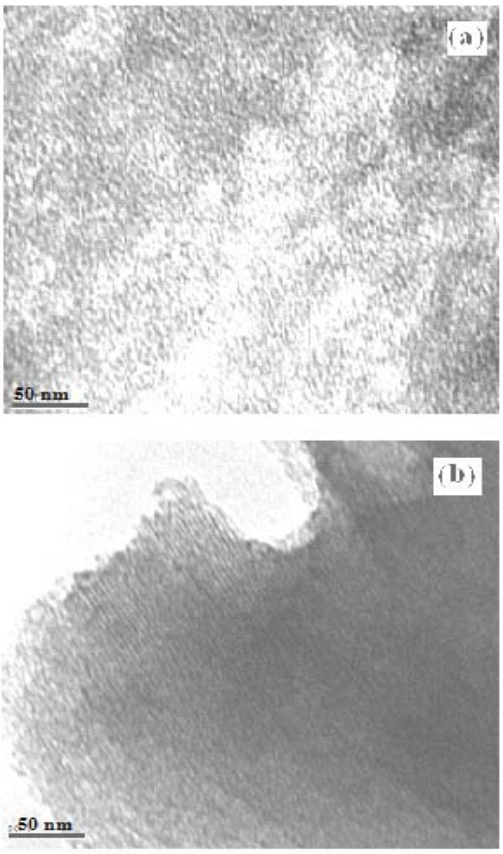

Figure 4. TEM images of MCM-41

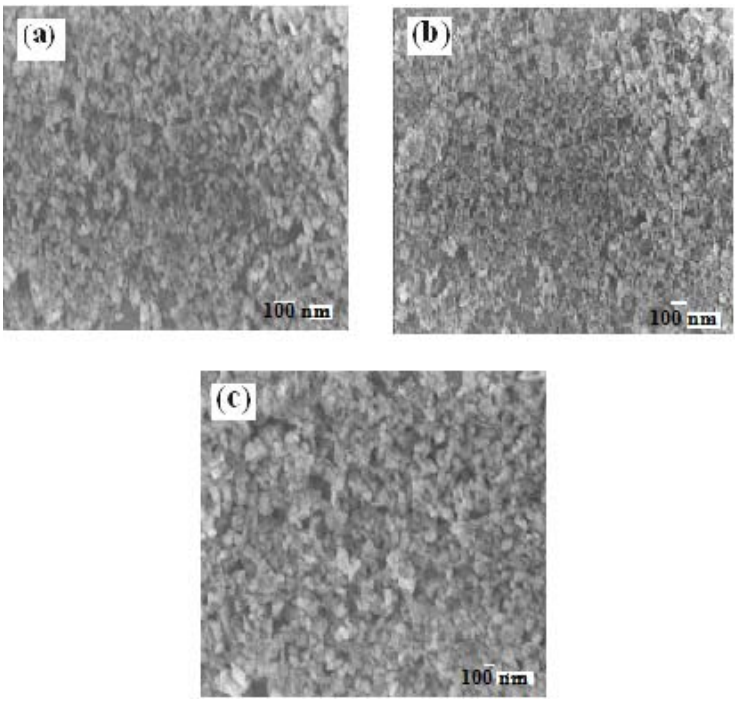

Figure 5. SEM images of (a) stainless steel, (b) copper and (c) nickel metal surfaces coated by mesoporous silicate (MCM-41) prepared by dipping method.

Corrosion measurement studies

Weight loss results at different temperatures. The weight loss measurements of the used electrodes in 2M HCl solution consuming three h for each run under different experimental conditions (temperature changes) are shown in Figures (6-9). The percentage of inhibition efficiencies (Table V) shows an increase in weight loss at increasing time and temperature. In case of coated samples, weight loss decreases compared to the uncoated samples indicating the ability of these compounds to inhibit corrosion.

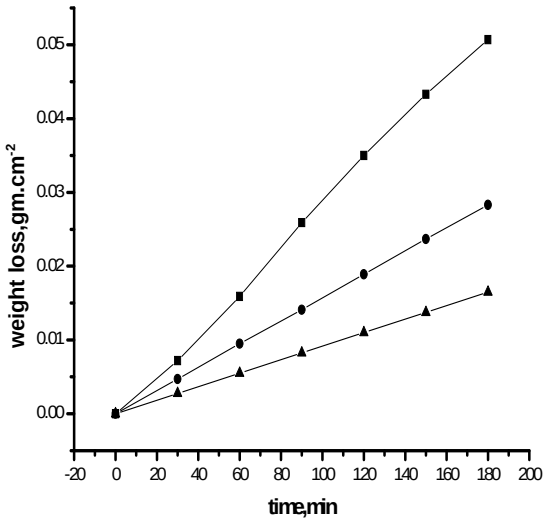

Figure 6. Weight loss vs. time curves for (■) 304 SS, (●) 304SS coated by SiO_2 and (▲) 304 SS coated by SiO_2 and poly-DSP in 2M HCl at 303 K.

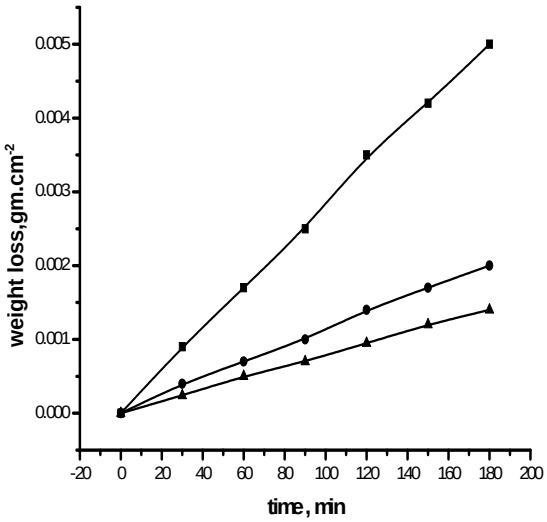

Figure 7. Weight loss vs. time curves for (■) 304 SS, (●) 304SS coated by SiO_2 and (▲) 304 SS coated by SiO_2 and poly-DSP in 2M HCl at 313 K.

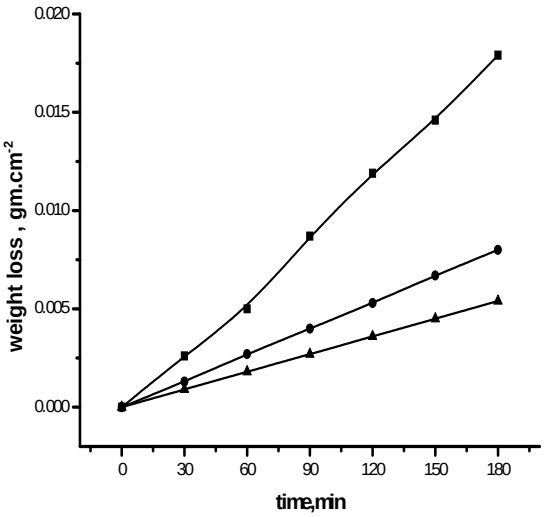

Figure 8. Weight loss vs. time curves for (■) 304 SS, (●) 304SS coated by SiO_2 and (▲) 304 SS coated by SiO_2 and poly-DSP in 2M HCl at 323 K.

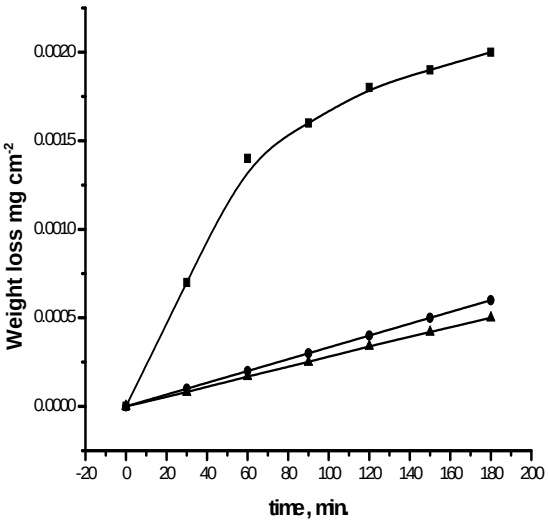

Figure 9. Weight loss vs. time curves for (■) 304 SS, (●) 304 SS coated by SiO_2 and (▲) 304 SS coated by SiO_2 and DSP in 2M HCl at 333 K.

TABLE V. Percentage of inhibition efficiencies (% IE), corrosion rates (R_{corr} mg.cm^{-2}.min^{-1}), and error bar in y-axis (yFr) of SiO_2 and poly-DSP coatings on 304 stainless steel by weight loss method at different temperatures.

Coating film	T K	R_{corr} mg.cm^{-2}.min^{-1}	yFr	% IE
SiO_2	303	0.15	1.50	70.0
SiO_2	313	0.40	1.44	60.0
SiO_2	323	2.00	1.38	55.0
SiO_2	333	7.07	1.34	44.2
SiO_2 and poly-DSP	303	0.12	1.40	75.0
SiO_2 and poly-DSP	313	0.36	1.20	72.0
SiO_2 and poly-DSP	323	1.35	1.10	69.8
SiO_2 and poly-DSP	333	4.13	0.88	67.4

Thermodynamic activation parameters measurement. The effect of temperature on the corrosion rates of stainless steel in 2M HCl solution is shown in Figure 10 for the uncoated and coated electrodes using weight loss measurements. The corrosion rate (R_{corr}) was calculated from the following equation (37).

$$R_{corr} = \Delta W / St \qquad [3]$$

where ΔW is the weight loss of metal in the corrosive solution, S is the surface area in cm^2 and t is the time in min. The results are depicted in Figures 10 for the investigated SiO_2 and poly-DSP coatings at temperatures 303, 313, 323 and 333K. It is clear from the results that the percentage of inhibition efficiencies decrease as the temperature increases.

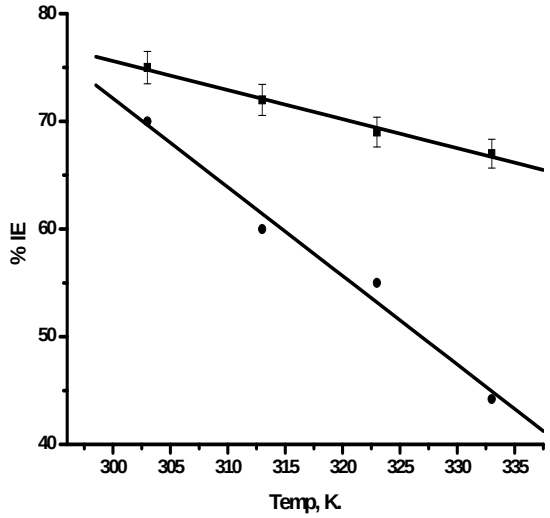

Figure 10. Variation of percentage of inhibition efficiency (%IE) with temperature of (●) 304 SS coated by SiO_2 and (■) 304 SS coated by SiO_2 and poly-DSP.

The apparent activation energies E_a of the corrosion reaction of the electrodes were calculated from Arrhenius equation (38).

$$R_{corr} = A \exp^{(-Ea/RT)} \qquad [4]$$

Figure 11 shows the Arrhenius plots of logarithmic values of corrosion rate; log R_{corr} vs. 1/T for 304 SS samples. The values of activation energy E_a were calculated from the slopes of the straight lines and are given in Table VI. The increase in the values of E_a is directly proportional to the inhibition efficiency of the nano-coatings. This indicates that the energy barrier of the corrosion reaction increases in presence of the surface layer material. This also indicates that such surface layers result in blocking of the active sites leading to an increase in the E_a values of the coated samples.

The free energy of activation $\Delta G^{\#}$ was calculated by applying the transition state equation.

$$\Delta G^{\#} = RT\,[\ln (kT/h) - \ln (\text{rate constant})] \qquad [5]$$

where: h is Planck's constant, k is Boltzmann's constant, R is the gas constant and T is the absolute temperature. The enthalpy of activation $\Delta H^{\#}$ and the entropy of activation $\Delta S^{\#}$ were calculated by applying the following equations:

$$\Delta H^{\#} = E_a - RT \quad [6]$$

$$\Delta S^{\#} = (\Delta H^{\#} - \Delta G^{\#})/T \quad [7]$$

It is clear from Tables (VII - IX) that the values of $\Delta G^{\#}$ and $\Delta H^{\#}$ increase with increasing temperature for the uncoated and coated electrodes, while $\Delta S^{\#}$ decreases with increasing temperatures. $\Delta G^{\#}$ is a thermodynamic parameter which indicates the tendency for an electrochemical reaction to occur spontaneously. The positive signs of $\Delta G^{\#}$ indicate that the reaction is non-spontaneous. The positive signs of $\Delta H^{\#}$ reflect the endothermic nature of the 304 stainless steel dissolution process. The large and negative values of $\Delta S^{\#}$ imply that the activated complex in the rate-determining step represents association rather than dissociation step, meaning that a decrease in disorder takes place on going from reactants to the activated complex.

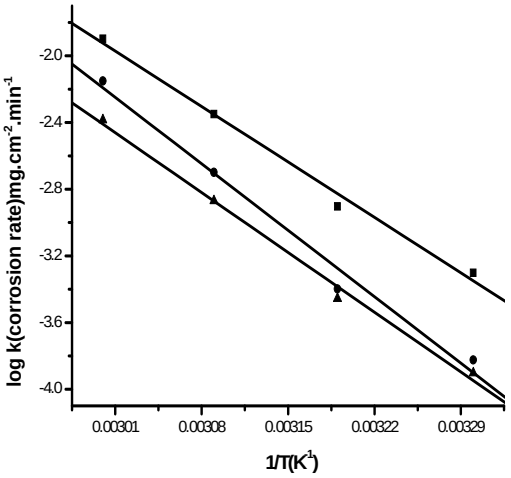

Figure 11. Arrhenius plots for corrosion of (■) 304 SS, (●) 304 SS coated by SiO_2 and (▲) 304 SS coated by SiO_2 and poly-DSP.

TABLE VI. Energies of activation of 304 stainless steel as determined by weight loss method in 2M HCl solution for 304SS, 304SS/SiO_2 and 304 SS/SiO_2/poly-DSP samples.

Electrode	E_a in kJ.mol^{-1}	% increase in E_a
Bare 304 SS	4.75	-
304 SS/ SiO_2	5.13	8
304 SS/SiO_2/poly-DSP	5.70	20

TABLE VII. Thermodynamic activation parameters for 304 stainless steel dissolution in 2M HCl solution.

Temp.(K)	303	313	323	333
Parameters	**Bare 304 SS**			
E_a kJmol^{-1}	4.75	-	-	-
$\Delta H^{\#}$ kJmol^{-1}	2.23	2.15	2.07	1.98
$-\Delta S^{\#}$ Jmol^{-1}K^{-1}	300.72	294.40	293.88	276.10
$\Delta G^{\#}$ kJmol^{-1}	93.35	93.91	94.13	97.17

TABLE VIII. Thermodynamic activation parameters for 304 stainless steel coated by SiO_2 in 2M HCl solution.

Temp. (K)	303	313	323	333
parameters		304 SS/SiO_2		
E_a kJmol^{-1}	5.13	-	-	-
$\Delta H^{\#}$ kJmol^{-1}	2.61	2.53	2.44	2.36
$-\Delta S^{\#}$ Jmol^{-1}K^{-1}	309.48	302.14	289.54	279.77
$\Delta G^{\#}$ kJmol^{-1}	95.53	95.96	96.38	97.10

TABLE IX. Thermodynamic activation parameters for 304 stainless steel coated by SiO_2 and poly- DSP in 2M HCl solution.

Temp.(K)	303	313	323	333
Parameters		304 SS/SiO_2/poly-DSP		
E_a kJmol^{-1}	5.70	-	-	-
$\Delta H^{\#}$ kJmol^{-1}	3.18	3.10	3.01	2.93
$-\Delta S^{\#}$ Jmol^{-1}K^{-1}	309.12	301.44	291.00	282.55
$\Delta G^{\#}$ kJmol^{-1}	96.84	97.02	97.02	97.44

Potentiodynamic polarization studies. Potentiodynamic polarization curves of metals were performed in the polarizing potential range from -2000 mV to 2000 mV (vs. SCE), at a scan rate of 10.0 mVs^{-1} in 2M HCl solution. The resulting current is plotted on logarithmic scale. The numerical values of the variation of corrosion current (I_{corr}), corrosion potential (E_{corr}), the slopes (α_a and α_c), corrosion rate (R_{corr}), and percentage of inhibition efficiency (% IE) in case of coated and uncoated samples are shown in Tables (X - XII). The cathodic and anodic curves exhibit Tafel-type behavior. In case of coated samples, both cathodic and anodic over voltages increase causing mainly parallel displacement to the more positive and negative values, respectively. Figures (12-14) show the corrosion behavior of the used electrodes under experimental conditions with a decrease in corrosion current density in case of coated samples. There are significant anodic and cathodic shifts of the corrosion potential to positive and negative values, respectively due to formation of protective layer. Tables (X - XII) show that Tafel constants (α_c and α_a) are changed in different manners. This may refer to different mechanisms in the way of corrosion inhibition. E_{corr} supplies an idea about the tendency of the material to corrode. If the corrosion potential of the coated steel is greater than that of the same steel uncoated, the coating induces a more "noble" behavior of the material and, thus, a less tendency to be corroded. Moreover, the passivity current density values give an idea of the rate of corrosion. In this way, lower values than those measured in uncoated metals indicate a more protective behavior of the investigated compounds or, in other words, a slower rate of corrosion (24).

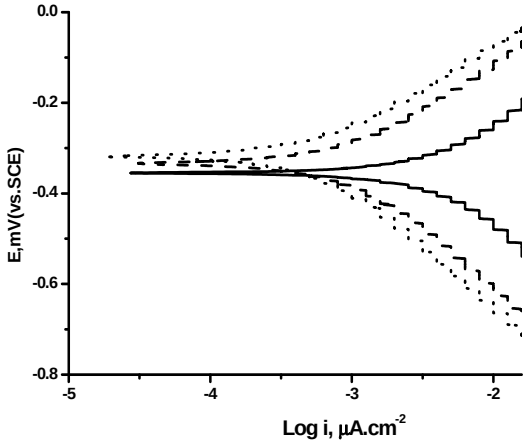

Figure 12. Polarization curves for (—) uncoated 304 SS, (--) 304 SS coated by SiO_2 and (…..) 304 SS coated by SiO_2 and poly-DSP.

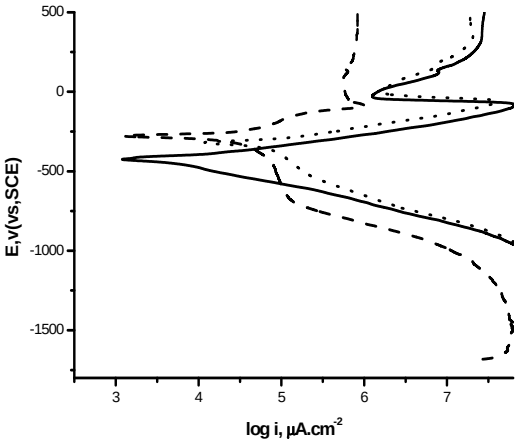

Figure 13. Polarization curves for (—) uncoated copper, (--) copper coated by SiO_2 and (…..) copper coated by SiO_2 and poly-DSP.

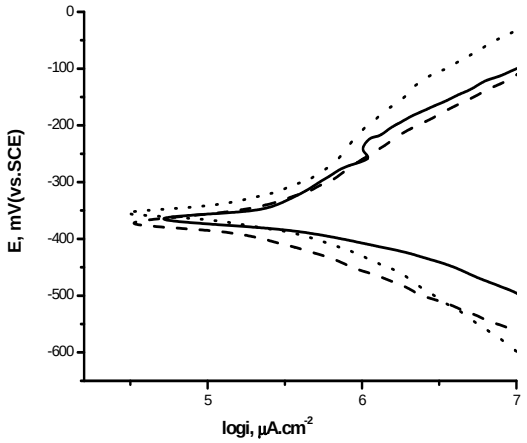

Figure 14. Polarization curves for (—) uncoated nickel, (--) nickel coated by SiO_2 and (…..) nickel coated by SiO_2 and poly-DSP.

TABLE X. Polarization parameters in the equivalent circuit for the uncoated and coated 304 stainless steel samples.

Electrode	E_{corr} (mV vs. SCE)	I_{corr} (mA/cm^2)	α_c mV/Decade	α_a mV/Decade	R_{corr} mm/yr	%IE
304 SS	-355	0.75	429	370	86.7	--
304SS /SiO_2	-334	0.10	283	220	12.2	85.9
304SS/SiO_2/poly-DSP	-318	0.06	273	200	7.08	91.9

TABLE XI. Polarization parameters in the equivalent circuit for the uncoated and coated copper samples.

Electrode	E_{corr} (mV vs. SCE)	I_{corr} (mA/cm^2)	α_c mV/Decade	α_a mV/Decade	R_{corr} mm/yr	%IE
Uncoated Cu	-250	0.031	-188	70.8	69.9	--
Cu/SiO_2	-260	0.006	-125	55.9	7.59	78.8
Cu/SiO_2/poly-DSP	-470	0.002	-98.5	53.6	2.72	92.4

TABLE XII. Polarization parameters in the equivalent circuit for uncoated and coated nickel samples.

Electrode	E_{corr} (mV vs. SCE)	I_{corr} (mA/cm^2)	α_c mV/Decade	α_a mV/Decade	R_{corr} mm/yr	%IE
Uncoated Ni	-350	0.402	-117	177	212	-
Ni/SiO_2	-340	0.171	-135	168	92.0	57.3
Ni/SiO_2/poly-DSP	-360	0.152	-63.3	139	61.9	61.9

Conclusion

We have prepared nano-SiO_2 coatings on metal surface by dipping method, and developed a hydrothermal post-treatment method to effectively eliminate the cracks and defects in the coating to optimize structure and properties for the coatings. Using distyryl pyrazine photopolymer through vapor deposition methods (CVD, PVD) we can form another film on silicate coatings to increase protection efficiency against corrosion. The results of chemical and electrochemical tests indicate that the hydrophobic coatings exhibit an excellent corrosion resistance in 2M HCl. The corrosion potentials shift positively, corrosion current density decreases, and the corrosion rate R_{corr} decreases. It is expected that the surface modification by nano-SiO_2 and poly-DSP coatings may become a promising technique in improvement of corrosion resistance of metals.

Acknowledgement

We acknowledge Prof. Dr. A. S. Fouda and Prof. Dr. M. A. Mohamed for making their corrosion facilities available to us

References

1. G. Grundmer, W. Schmidt and M. Stratman, *Electrochimica Acta.*, **45**, 2515 (2000).

2. R. Haneda and K. Aramaki, *J. Electrochem. Soc.,* **145**, 2786 (1998).
3. W. Lu, R. L. Elsen, T. Chen and V. L. Kul, *Mat. Res. Soc. Symp. Proc.,* **488**, 653 (1998).
4. M. Guglielm, *J. Sol-Gel Sci. Tech.,* **1**, 177 (1994).
5. D. Vascon, J. Carva, M. Mantel and W. Vasconce, *J. Non-Cryst. Solids,* **273**, 135 (2000).
6. M. Simoes, O. Assis and L. Avaca, *J. Non-Cryst. Solids,* **273**, 159 (2000).
7. M. Atik, S. H. Messa, F. P. Luna and M. A. Agerter, *J. Mater. Sci. Lett. ,* **15**, 2051 (1996).
8. P. Neto, M. Atik, L. A. Avaca and M. A. Agerter, *J. Sol-Gel Sci. Tech.,* **2**, 529 (1994).
9. C. J. Brinker and G. W. Scherer, *Sol-Gel Science*: *The physics and Chemistry of Sol-Gel Processing*, Academic Press, San Digo, CA (1990).
10. A. C. Pierre, *Introduction to Sol-Gel Processing*, Kluwer, Boston, MA (1998).
11. L. F. Francis, *Mater. Manufacturing Process.,* **12**, 963 (1997).
12. X. H. Han, G. Z. Cao, T. Prat, T. D. Schwa and B. Lutz, *J. Mater. Sci.,* **36**, 985 (2001).
13. C. M. Chan, H. Fong, M. Sarika and T. Robinson, *J. Mater. Res.,* **15**, 148 (2000).
14. J. Wen and G. L. Wilkes, *J. Inorganic and Organometallic Polymers.,* **5**, 343 (1995).
15. J. S. Park and J. D. Mackenz, *J. Amer. Ceram. Soc.,* **78**, 2669 (1995).
16. S. H. Messa, S. H. Pulcine and A. C. Guasta, *J. Non-Cryst. Solids,* **247**, 164 (1999).
17. A. Atik, F. P. Luna ans S. H. Messa, *J. Sol- Gel. Sci. Tech.,* **8**, 517 (1997).
18. C. Liu, Q. Bi and A. Matthews, *Corros. Sci.,* **10**, 1953(2001).
19. K. L. Choy, *J. Mater. Sci.,* **48**, 57 (2003).
20. G. S. Vicente and M. T. Gutierrez, *Thin Solid Films.,* **404**, 335 (2002).
21. U. Erb, *J. Nonstruct. Mater.,* **6**, 533 (1995).
22. Q. W. Li, H. P. Pei, X. Nan, et al., *J. Matter. Sci.,* **173**, 263 (2000).
23. J. Masalaki, J. Gluszek, J. Zabrzeski, et al., *Thin Solid Films,* **349**,186 (1999).
24. S. Shakka, H. Kozuka, *Handbook of Sol Gel Science and Technology,* p. 400, Kluwer Academic Publication, UK (2005).
25. S. Sathiyan, S. Azim and G. Venkat, *J. Electrochimica Acta.,* **52**, 2068 (2007).
26. P. J. Kinlen and V. Y. Menon, *J. Electrochem. Soc.,* **146**, 3690 (1999).
27. P. J. Kinlen and Y. Ding, *D. C. Silverman Corrosion.,* **58**, 490 (2002).
28. S. A. Umoren and E. E. Ebenso, *Pigment & Resin Technology.,* **35**(6), 346 (2006).
29. Y. k. Ueda, *J. Crystal Growth.,* **113**, 69 (1991).
30. T. Kokubo, H. Kushitani and S. Sakka, *J. Biomed. Mater. Res,* **24**, 721 (1990).
31. H. M. Probst and H. C. Hanack, *Synthesis and Characterization of Pyrazine,* p. 34, Bangkok, Thailand (2001).
32. M. Hasegawa, *New Polymerization Reactions*, p. 1, Springer Berlin, Heidelberg (1982).
33. E. P. Barrett, L. G. Joyner and P. P. Halenda, *J. Am. Chem. Soc.,* **73**, 373 (1951).
34. M. A. Elmorsi, *Corros. Sci.,* **41**, 304 (1999).
35. M. Ahola, P. Kortesuo and I. Kangasn, *Drug Dev. Ind. Pharm.,* **25**(8), 955 (1999).
36. P. Kortesuo, M. Ahola and S. Karlsson, *J. Biomed. Mater. Res,* **44**(2), 162 (1999).
37. F. Bensa, S. Alehyen and M. ElAcho, *Anticorros. Methods and Mater.,* **50**, 402 (2003).

38. Q. W. Atkins, *Physical Chemistry*, 5th Ed., p. 8, Oxford University Press: Oxford (1994).